LASER INTERFEROMETER GRAVITATIONAL WAVE OBSERVATORY
- LIGO -
CALIFORNIA INSTITUTE OF TECHNOLOGY
MASSACHUSETTS INSTITUTE OF TECHNOLOGY

Technical Note **LIGO-T1300555-v1-** 2013/10/06

Implementing an Angular Sensing and Control (ASC) System for the 40m Prototype Interferometer

Gautam Venugopalan
Mentors: Manasadevi P Thirugnanasambandam, Jenne Driggers, Rana Adhikari

California Institute of Technology
LIGO Project, MS 18-34
Pasadena, CA 91125
Phone (626) 395-2129
Fax (626) 304-9834
E-mail: info@ligo.caltech.edu

Massachusetts Institute of Technology
LIGO Project, Room NW22-295
Cambridge, MA 02139
Phone (617) 253-4824
Fax (617) 253-7014
E-mail: info@ligo.mit.edu

LIGO Hanford Observatory
Route 10, Mile Marker 2
Richland, WA 99352
Phone (509) 372-8106
Fax (509) 372-8137
E-mail: info@ligo.caltech.edu

LIGO Livingston Observatory
19100 LIGO Lane
Livingston, LA 70754
Phone (225) 686-3100
Fax (225) 686-7189
E-mail: info@ligo.caltech.edu

http://www.ligo.caltech.edu/

Abstract

Laser Interferometer Gravitational-Wave Observatory (LIGO) detectors are extremely sensitive to the angular orientation of the interferometer test masses. Fluctuations in the angular orientation of these test masses adversely affects laser power build-up in the various Fabry-Perot cavities that constitute the interferometer, and the beam centering on mirrors. In this project, an Angular Sensing and Control (ASC) system is commissioned for the auxiliary laser beam at a 40m prototype interferometer. The system consists of piezoelectrically controlled steering mirrors that direct the auxiliary beam into the Fabry-Perot arm cavity. These actuators, once calibrated, are integrated with a software-based remote monitoring and control environment in which a software servo is implemented to feedback to the steering mirrors. This allows stable power build-up in the interferometer and precise input pointing of the auxiliary laser beam into the interferometers arm cavities.

Acknowledgements

I would like to express my sincere gratitude towards my mentor, Dr. Manasadevi Thirugnanasambandam, for all the insight and guidance offered during the course of this project. I would also like to thank my co-mentor, Jenne Driggers for bearing with my questions, and Prof. Rana Adhikari for giving me the opportunity to work on things outside of my project, keeping me occupied through the summer.

I also had the privilege of working with a large number of people involved with the LIGO project, both at the 40m and at West Bridge. I would like to thank all of them (Dr. Jameson Rollins and Dr Koji Arai in particular) for their help and advice.

The summer of 2013 was my second experience working with a gravitational wave detector, and I would like to thank Dr. Jonathan Leong and Dr. Hartmut Grote from GEO 600 for making my first experience thoroughly enjoyable and for motivating me to pursue another summer with LIGO.

I would also like to thank Professor S Kasiviswanathan, my faculty advisor, for being thoroughly supportive of me, and for helping me work around the numerous administrative formalities such that I could grab this incredible opportunity.

Finally, I would like to thank the SURF community, the Student Faculty Programs Office, LIGO, the NSF, and IIT Madras for giving me the opportunity to work at Caltech for 10 weeks. It was one of the most enriching learning experiences I have had.

Contents

1 Introduction **7**

2 The Problem, Project Objectivesm and Approach **8**

2.1 The Problem 8

2.2 Project Objectives 8

2.3 The Approach 9

3 Implementation **10**

3.1 Optical Layout of the Upgraded Y-Endtable of the 40m Interferometer . . . 10

3.1.1 The Auxiliary laser system 11

3.2 Mode-matching the Auxiliary laser to the FP arm cavity 12

3.2.1 Gaussian beam propagation 12

3.2.2 Mode-matching a laser beam to an optical cavity 13

3.3 Pound-Drever-Hall (PDH) locking the auxiliary laser to the cavity 17

3.4 Electronics for the ASC Servo 20

3.4.1 PZT driver boards 23

3.4.2 Digital-to-Analog Converter (DAC) 24

3.4.3 Anti-Imaging (AI) Boards 25

3.4.4 High Voltage DC Power Supply 26

3.5 Optics for the ASC Servo 27

3.5.1 Mounting the Steering Mirrors onto the Piezoelectric Tip-Tilts 27

3.5.2 Calibrating the Piezo-Mounted Mirror 28

3.6 Designing the Control and Data-Acquisition System (CDS) for the ASC Servo 30

4 Measurements for Optimizing CDS Servo and Results **32**

4.1 Dither Signal Parameters 33

4.2 Gains and Cut-Off Frequencies of Lock-In-Amplifier Filters 33

4.3 Control Filters 34

4.4 Input and Output Matrices 34

4.5 Results and Servo Performance 35

5 Concluding Remarks and Future Work **35**

6 Appendix **37**

6.1 MEDM screens 37

List of Figures

1 Diagram of a Michelson Interferometer (with Power Recycling and Fabry Perot (FP) Arm Cavities) for gravitational wave detection [3] 7

2 Transmitted Power of Auxiliary laser beam as a function of x-displacement of interferometer mirror (Top), and its derivative (Bottom) 10

3 The Proposed Servo Design 11

4 Main elements of the Auxiliary laser system [14]. 12

5 Propagation of a Gaussian beam. The beam waist is marked w_o 13

6 Propagation of a beam through an optical component 13

7 Mode-matching solution given by A La Mode. The origin of the coordinate system is the end of the second Faraday isolator in the beam path as shown in Figure 4 , while the target beam waist is 2.152 mm and is located at ITM Y. 15

8 Beam propagation from the end of the Faraday isolator to the ETM. Mode-matching lenses are marked. 16

9 Physical layout of components on the endtable. 16

10 The general layout for locking the auxiliary laser to the FP arm cavity. Part of the incident light from the auxiliary laser is transmitted through the ETM and is resonant in the cavity, while part of it gets reflected. The reflected beam is rejected by the Faraday isolator and serves as the error signal for the PDH loop. 17

11 A plot of the PDH error signal [12]. The error signal goes to zero whenever any of the three incident beams (carrier and two sidebands) is resonant inside the cavity. 18

12 The circuit schematic for our model of the path from the LO to the Universal PDH box. The output impedance of the LO and the input impedance of the Universal PDH box are assumed to be 50 Ω. The value of the capacitance is swept through different values in the simulation. 19

13 Results of the simulation, for various values of the capacitance C1. 20

14 Block diagram of the scheme used to measure the transfer function of the PDH loop. The quantity measured by the spectrum analyzer is a1/a2, which works out to be the open loop transfer function. 21

15 Measured open-loop transfer function of the PDH loop. The UGF of the loop is $\approx 11.7kHz$ 21

16 Wiring diagram outlining the various parts of the ASC servo. The error signal is the transmitted green beam from the arm cavity, monitored at the PSL table with a photodiode and taken into the digital domain by an Analog-to-Digital Coverter (ADC). The software ASC servo then filters the error signal, and outputs a digital feedback signal, which is converted back into an analog signal by a Digital to Analog Converter (DAC). This signal then goes through an Anti-Imaging (AI) board to a PZT driver board which then sends the feedback signal to the two piezoelectric tip-tilts on which the steering mirrors are glued. 22

17 Amplifying stage on the PZT driver board is highlighted in blue. The 100 V DC bias voltage is supplied via a high-voltage power supply. 23

18 Results of the test to verify the output amplitude range of the DAC. Traces are labelled. The output voltage swings between -10V and 10V (both with respect to ground). 24

19 Power Spectral Density (PSD) of DAC channel 9 while a 2 kHz, 1000 counts amplitude sine wave was being output from it. The peak at $\approx 64kHz$ is marked. 25

20 Measured transfer function of a modified channel on the AI board, in comparison to the original configuration. The position of the notches (both original and modified) are marked. 26

21 2-inch CVI mirror with HR and AR coatings for 532 nm in a modified Newport U100-P mirror mount, on a 2.5-inch optical post. 27

22 Schematic representation of the setup used to calibrate the PZT. The laser source is a red He-Ne laser, which is reflected by the piezo-mounted mirror onto the QPD, which can track the change in the spot position in response to the steering mirror being tilted. The input signal to the PZT is supplied by a function generator through the PZT driver board. The high-voltage power supply delivers a stable, 100V DC bias voltage. 28

23 QPD Calibration Curves 29

24 PZT Calibration Curves 31

25 Full-range calibration of PZT mounted mirror 1 31

26 Full-range calibration of PZT mounted mirror 2 31

27 Schematic of the CDS signal chain. The error signal from the X-arm green transmission photodiode (GTRX PD) is acquired into the CDS and demodulated by a stage of Lock-In-Amplifiers. The demodulated signal is fed to the control filters via an Input Matrix. The feedback signal is then sent to an Output Matrix, summed with the Local Oscillator signal and a DC bias signal (if any) to the PZT mounted mirrors. 32

28 Angular misalignment of the beam axis with respect to the cavity axis. . . . 33

29 Power Spectral Density of the X-end Green Transmission Photodiode (GTRX) signal. Note that the Y-axis is the Relative Intensity Noise (RIN). 34

30 Performance plot for the ASC servo. Key events are marked on the plot. The test itself is described in detail below. 35

31 MEDM screens that constitute the ASC Servo 38

1 Introduction

Einstein's theory of general relativity has been successful in providing a satisfactory theoretical framework which explains several physical phenomena that Newtonian physics was not able to. One of the predictions of the theory of general relativity is the gravitational wave. Measurement and characterisation of gravitational waves will be another empirical observation in support of this theory.

The physical manifestation of gravitational waves is a strain in space-time, which from a field-theory perspective can be modelled as a perturbation to the 4-dimensional Minkowski metric [1]. Measurement of this strain would then allow the characterisation of the gravitational wave. The primary difficulty in directly measuring a gravitational wave is the length-scale of the problem, set by the ratio of the universal gravitational constant, G and the fourth power of the speed of light, c [1].

$$h \sim G/c^4 \sim 8.23 \times 10^{-45} m^{-1} kg^{-1} s^2 \tag{1}$$

Thus, any attempt to measure the effects of a gravitational wave has to employ an instrument that is sensitive to extremely small strains. One such class of instruments, capable of measuring very small changes in length, are laser interferometers [2]. A schematic of how an interferometer is used to measure strain due to gravitational waves is depicted in Figure 1.

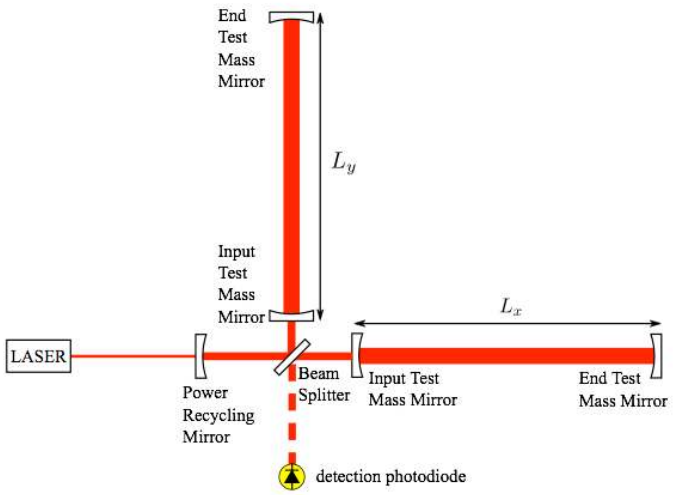

Figure 1: Diagram of a Michelson Interferometer (with Power Recycling and Fabry Perot (FP) Arm Cavities) for gravitational wave detection [3]

The end mirrors of the interferometer can be considered as free masses, which will be displaced by a passing gravitational wave. As the two arms of the interferometer are orthogonal to each other, an incident gravitational wave results in a phase difference $\Delta\phi$ (which is proportional to the differential arm length $L_x - L_y$) between the waves arriving at the Beam-Splitter from both arms.

Hence, the intensity of the recombined light is a function of the differential arm length (DARM) of the interferometer, and therefore, the intensity of the light at the detection port is proportional to the gravitational wave strain. While this scheme is simple enough in principle, there are a number of difficulties in commissioning an interferometer to detect gravitational waves.

2 The Problem, Project Objectivesm and Approach

2.1 The Problem

The difficulties involved in building a gravitational wave detector can be classified into two principal categories; those arising from the electronics used to track the intensities at the output ports and those arising from the interferometer parts themselves (mirrors, beam-splitters etc). We will be primarily concerned with the latter.

The difficulty is the following; if we are to indeed ascribe a change in the intensity at the output ports of the interferometer to a gravitational wave-induced strain, then it must be true that any change in the DARM must have been due to the gravitational wave alone. It is implicitly assumed that in the absence of a gravitational wave, the interferometer is perfectly stationary. Naturally, this assumption is not a valid one in a practical implementation of an interferometer, as there are various sources which corrupt the detector output.

Of the various degrees of freedom of the interferometer, the angular ones are particularly important. Not only do they couple to the DARM, but angular misalignment also affects the ability of the the coupled cavities of the dual power-recycled Michelson interferometer to remain resonant to the main laser beam. Maintaining the angular positions of the mirrors is critical if this is to be attained. Thus, reducing unwanted angular motion is an important milestone in increasing the sensitivity of the LIGO detectors.

A number of control loops are common in interferometers. These loops sense undesirable movements of the mirrors in the interferometer (from various sources), process this information and appropriately actuate on the mirrors to counteract the movement such that the interferometer as a whole remains stationary.

2.2 Project Objectives

Alignment Sensing and Control (ASC) systems have been successfully commissioned before, and their performance has been evaluated in detail [3]. In designing an ASC system, the important steps are the following:

- Identify points from which the error signal is to be sensed.
- Digitize the error signal and filter it appropriately.
- Derive a feedback signal.
- Actuate using this feedback signal.

Usually, the points of actuation are the various mirrors in the cavities themselves. Implementing an ASC in this manner, however, is a formidable task as there is a fairly complex, non-linear coupling between the various cavities in the interferometer that has to be taken into account.

2.3 The Approach

The approach to be taken in this project is as follows. Two auxiliary laser beams, each located at one end-station of the interferometer (near the "End Test Mass Mirrors" in Figure 1) output beams at 1064 nm. This light is then doubled in frequency to create a 532 nm beam. A control loop (explained below) will make use of the 532 nm beam to ensure that the cavity is locked to the auxiliary laser beam. The 532 nm beam serves as a sensor for measuring the angular alignment for the Fabry-Perot arm cavity. The advantage of such an approach is that we are injecting the beam through the end-mirrors of the interferometer, avoiding the coupled cavities around the beam splitter, and so get information only about our arm cavity. Thus, we avoid the aforementioned non-linear coupling between the various cavities in the interferometer.

The other pertinent point about the proposed ASC is that there is no actuation on any of the interferometer mirrors. Rather, the proposed servo actuates on a set of steering mirrors that are used to guide the auxiliary laser beam into the cavity. Any misalignment in the cavity will mean that it is no longer perfectly resonant for the 532 nm auxiliary beam. Using the intensity of transmitted light at 532 nm as a measure of whether the cavity is ideally aligned to the auxilary laser or not, we are able to actuate on the mirrors that steer the auxiliary laser into the cavity such that it remains locked to the 532 nm beam.

The power of the transmitted light from a cavity is maximum when the cavity axis and the transmission axis of the laser beam coincide perfectly. When this alignment is disturbed, the transmitted power falls. A detailed mathematical treatment of this in terms of eigenfunctions of the cavity may be found in [4] or [5], but a qualitative picture can be derived from the sketches shown in Figure 2.

The inverted parabola in the top plot in Figure 2 is representative of the transmitted power as a function of the displacement of the centre of an interferometer mirror in (say) the x-direction with $x = 0$ corresponding to the cavity being perfectly aligned. A difficulty becomes immediately apparent-because the graph is symmetric about $x = 0$, we need a means of sampling the derivative of this function in order to actuate correctly on the steering mirrors. To help solve this problem, a modulation signal is introduced in the servo loop.

The actuators used to move the steering mirrors are essentially piezoelectric transducers, made of Lead Zirconate Titanate (henceforth referred to as PZTs). PZTs respond to an applied voltage by a change in its physical dimensions, which is the mechanism by which they actuate the steering mirrors.

The signal applied to the PZTs on the steering mirrors is a combination of the feedback signal and a small amplitude modulation signal, at frequency ω_o. A photodiode measures the transmitted power of the 532 nm beam, and a band-pass filtering stage allows us to extract the error signal at the frequency of the modulation signal.

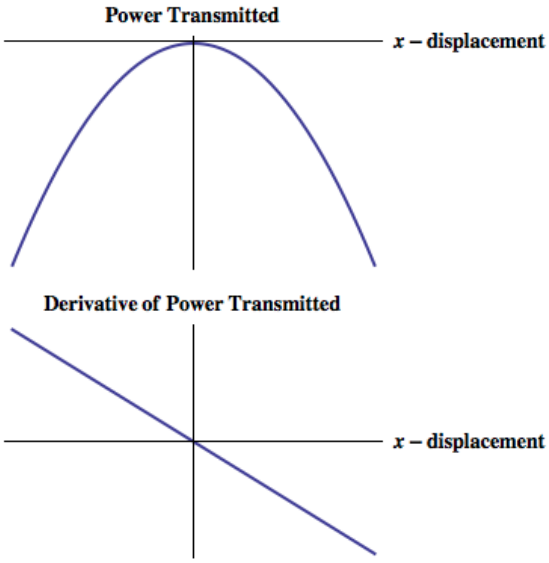

Figure 2: Transmitted Power of Auxiliary laser beam as a function of x-displacement of interferometer mirror (Top), and its derivative (Bottom)

By demodulating the error signal with the modulation signal, and comparing the phase of the demodulated signal with that of the Local Oscillator signal, we get information about which side of the origin we are on.

Knowing the transfer function of the system, we can design a set of control filters, derive a feedback signal which will be fed to the PZTs. The feedback signal undergoes a low-pass filtering operation to ensure that only the first harmonic of the demodulated signal is sent to the PZTs.

A block diagram of the proposed servo, with all the elements explained above included, is shown in Figure 3.

3 Implementation

In the previous sections, the conceptual framework behind this project has been described. In this and subsequent sections, we shall discuss aspects pertaining to the implementation of an ASC system, and the progress made thus far in this respect.

3.1 Optical Layout of the Upgraded Y-Endtable of the 40m Interferometer

The optical tables holding the auxiliary green laser are, at the time of writing, undergoing an upgrade in order to allow better stability and input pointing of the Arm Length Stabilization (ALS) system. Work is proceeding independently on the X and Y arms of the interferometer.

ASC is primarily concerned with the auxiliary laser and the main elements of this system are illustrated schematically (the actual layout of the components on the table are different)

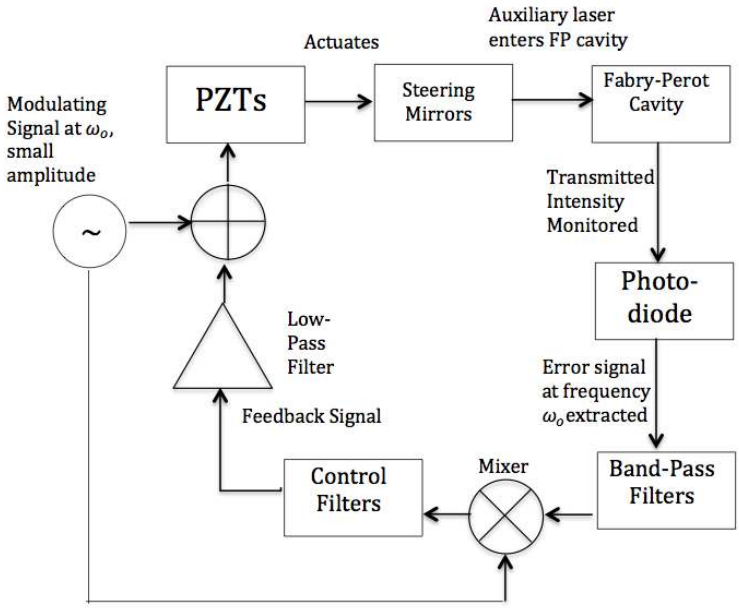

Figure 3: The Proposed Servo Design

in Figure 4 for greater clarity. These components have been divided into two sections; one which deals with the polarization of the beam and the second harmonic generation, and the other which is used to mode-match the auxiliary beam to the cavity.

3.1.1 The Auxiliary laser system

The first stage consists of components used to derive an appropriately polarized green beam from the auxiliary laser. The auxiliary laser is a Non-Planar Ring Oscillator (NPRO) that resonates at 1064 nm. The main beam in the interferometer is p-polarized and hence, all the optics in the main interferometer are chosen to work with p-polarized light. The combination of the Quarter-Wave-Plate (QWP) and Half-Wave-Plate (HWP) ensures that the auxiliary laser beam too is p-polarized.

The first of two Faraday isolators in this system (designed for 1064 nm light) ensures that no light is reflected back into to the NPRO. The 1064 nm beam then enters a second harmonic generation (SHG) crystal which doubles the frequency of the incident light and emits a beam composed of light at 1064 nm and 532 nm. A harmonic separator rejects the 1064 nm content. The beam then enters a second Faraday isolator (designed for 532 nm light).

The second stage consists of optics used to mode-match the green laser to the FP arm cavity. There are two mode-matching lenses which allow the shaping of the beam as it propagates (discussed in greater detail in the next section). The beam then enters the FP arm cavity, while the rejcted beam from the Faraday isolator is steered using a mirror to a photodiode. This signal serves as the error signal for Pound-Drever-Hall (PDH) locking of the auxiliary laser to the cavity.

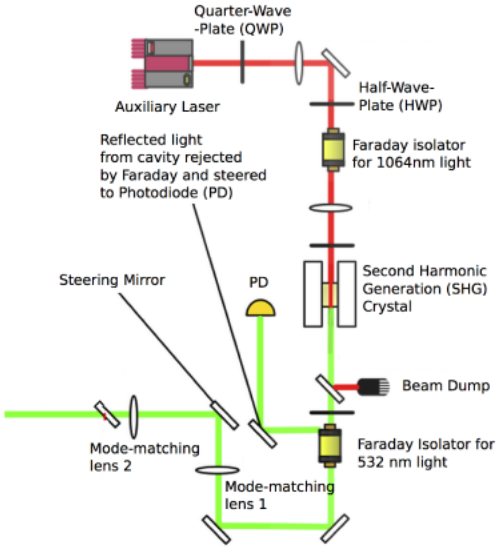

Figure 4: Main elements of the Auxiliary laser system [14].

3.2 Mode-matching the Auxiliary laser to the FP arm cavity

Before the mirrors could be installed on their PZT mounts, the green beam had to be mode-matched to the FP arm cavity. Gaussian beam propagation and mode-matching techniques are briefly discussed in this section. Also described is how we attempted to find a mode-matching solution that met our requirements.

3.2.1 Gaussian beam propagation

The auxiliary laser is oscillating in the TEM_{00} mode [9] which means that it emits a beam that has a transverse intensity profile that can be modelled using Gaussian functions. If the beam is propagating along the $z-$direction, then its intensity profile in a plane transverse to the direction of propagation (i.e. the $x-y$ plane) may be modelled as

$$I(r,z) = I_o(z)e^{-2r^2/w^2(z)} \tag{2}$$

where $I_o(z)$ is the peak intensity at z, r is the transverse radial distance from the $z-$axis, and w is that radial distance at which the intensity drops to $I_o(z)e^{-2}$. Thus, practically all the energy in the beam is contained within an imaginary cylindier of radius w[2], and when we speak of the spot-size of the beam, it is really a circle of radius w that is being referred to. The minimum value attained by w is called the beam-waist, and is denoted by w_o

Figure 5 illustrates the propagation of a Gaussian beam as well as the location of the beam waist. The propagation of such a Gaussian beam is modelled by the following equation (setting the position of the beam-waist at $z = 0$):

$$w(z) = w_o[1 + (\frac{\lambda z}{\pi w_o^2})^2]^{1/2} \tag{3}$$

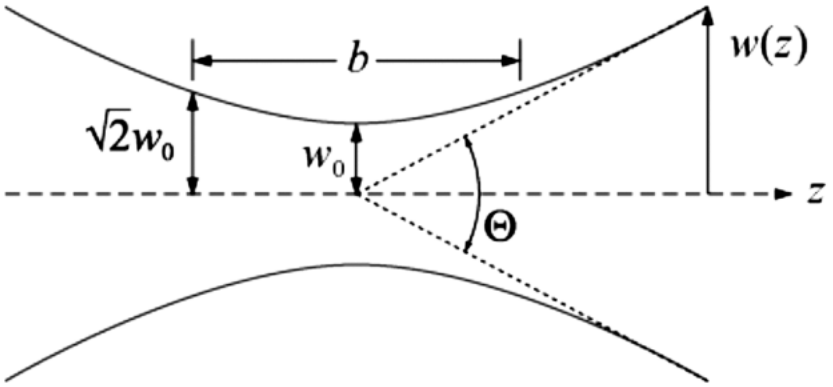

Figure 5: Propagation of a Gaussian beam. The beam waist is marked w_o

It is desirable to have control over the location of the beam waist and the spot size of the beam at various points along its path. In particular, the beam entering the FP arm cavity must be such that it is resonant within the cavity. This is done using a combination of lenses placed at specific locations on the beam path. The procedure is called mode-matching.

3.2.2 Mode-matching a laser beam to an optical cavity

The propagation of Gaussian beams through optical components such as lenses and optical cavities can be modelled using transfer matrices under the paraxial approximation [10]. These transfer matrices are commonly referred to as ABCD matrices by virtue of them being 2-by-2 matrices whose elements are characteristic of the optical component and its position. When multiple optical components are present, the ABCD matrix characterising the compound optical system can be obtained by multiplying the individual components' ABCD matrices.

Figure 6 illustrates the propagation of a beam through an optical component.

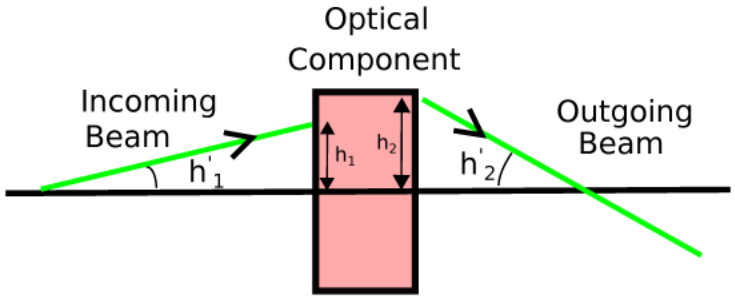

Figure 6: Propagation of a beam through an optical component

The transfer matrix relation for the situation depicted in Figure 6 is as follows;

$$\begin{bmatrix} h_2 \\ h_2^{'} \end{bmatrix} = \begin{bmatrix} A & B \\ C & D \end{bmatrix} \begin{bmatrix} h_1 \\ h_1^{'} \end{bmatrix} \tag{4}$$

Thus, knowing the ABCD matrix for a given optical component, and the parameters characterising the incoming beam (h_1 and $h_1^{'}$), we can calculate the parameters characterising the output beam.

In attempting to mode-match the green beam from the auxiliary laser to the FP cavity, we had to find a combination of lenses that results in a beam of the desired profile entering the cavity. In reality, this is a complex optimization problem which does not have a unique solution. The problem was further complicated by the fact that there are 5 optical components in the compound system, namely three lenses, the ETM and the ITM. Of these, the positions of the ETM, ITM and one lens is fixed. The goal then was to find two lenses of suitable focal lengths and put them in the right positions such that the waist of the beam in the cavity was at the ITM, which was necessary for the auxiliary laser beam to be resonant in the TEM_{00} mode within the FP arm cavity.

We used a MATLAB package called 'a la mode' [11] to solve this optimization problem. The input parameters fed into the script were the characteristics of the input beam (i.e. the beam from the second Faraday isolator shown in Figure 4), the position and size of the desired beam-waist, positions of the fixed optical elements, and a list of available lenses to choose from.

Despite the package simplifying the computation significantly, realizing this solution physically was a challenging task due to the following reasons:

- The MATLAB package assumes thin lenses which is an idealization of the actual scenario, where the lenses have finite thickness.
- A la mode is very sensitive to the inital values fed to it, as well as the tolerances used to reject candidate lens combinations. Thus, it is difficult to systematically identify the 'best' solution as different initial conditions and tolerances tend to yield different solutions.
- The auxiliary laser intensity profile is assymetric, whereas in the script it is assumed to be circular.
- The alignment of the steering mirrors was crucial in determining if the right mode-matching solution had been realised. Even with the right lenses at the right place, an improperly aligned beam going into the interferometer would mean that the beam would resonate at some higher order mode than the desired TEM_{00}.

We adopted the following measures:

- In order to minimize the effect of the non-ideality of the lenses, we placed the first lens at the location where the spot size of the actual beam matched that in the MATLAB simulation. We then fine-tuned the position of the lens such that the beam emerging from it had the same size as the corresponding beam in the simulation. This effectively simplified the problem to accurately positioning one lens.

- Of the candidate solutions obtained, we chose the combination of lenses that was least sensitive to the position of the second lens, which was the one that had to be tuned. A la mode parametrizes sensitivity to the position of a lens using its axial displacement matrix element, A.

  The power P remaining in the TEM_{00} mode if an optical component with axial displacement matrix element A is displaced through Δz is $P = 1 - (A\Delta z)^2$. Thus, the solution chosen had the smallest sensitivity among all the candidate solutions for the second of the two mode-matching lenses (marked L2 in Figure 7).

- In order to account for an assymetric beam, the square-root of the x and y beam radii were fed into the simulation.

The eventual solution we used is shown in Figure 7, which is zoomed in Figure 8 so as to show the beam propagation between the origin and the ETM. The two mode-matching lenses have focal lengths of 15 cm (lens 1) and 25 cm (lens 2). The numbers shown are from the simulation, and some tuning of the positions of the two lenses had to be done in order to realise the solution.

The actual layout on the optical table is shown on the left in Figure 9, with the mode-matching lenses marked. The path taken by the rejected beam from the Faraday isolator, which serves as the error signal for the PDH servo that locks the auxiliary laser to the cavity, is shown in the figure on the right.

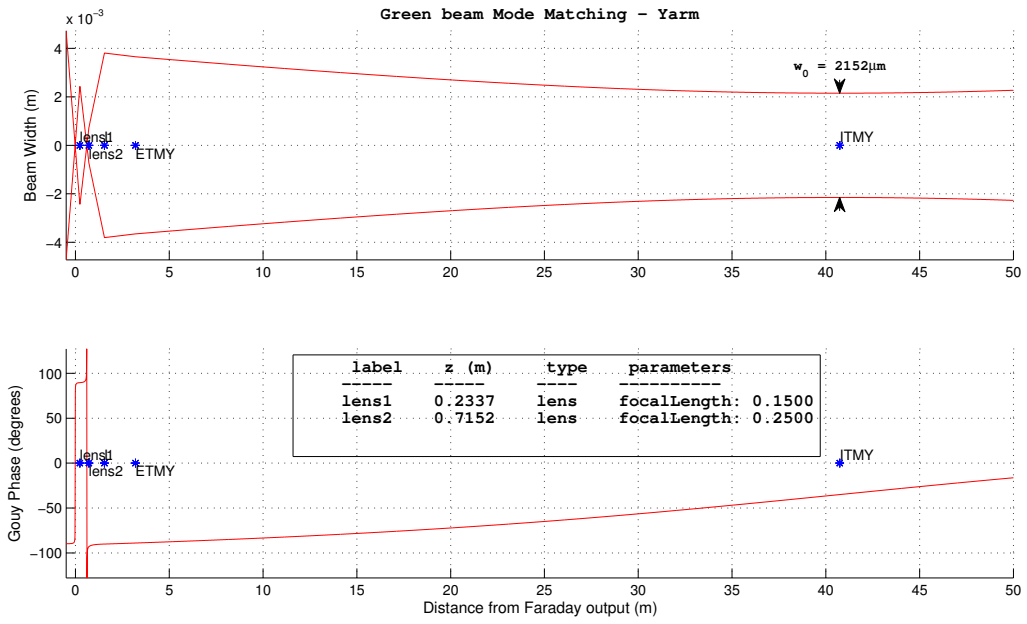

Figure 7: Mode-matching solution given by A La Mode. The origin of the coordinate system is the end of the second Faraday isolator in the beam path as shown in Figure 4 , while the target beam waist is 2.152 mm and is located at ITM Y.

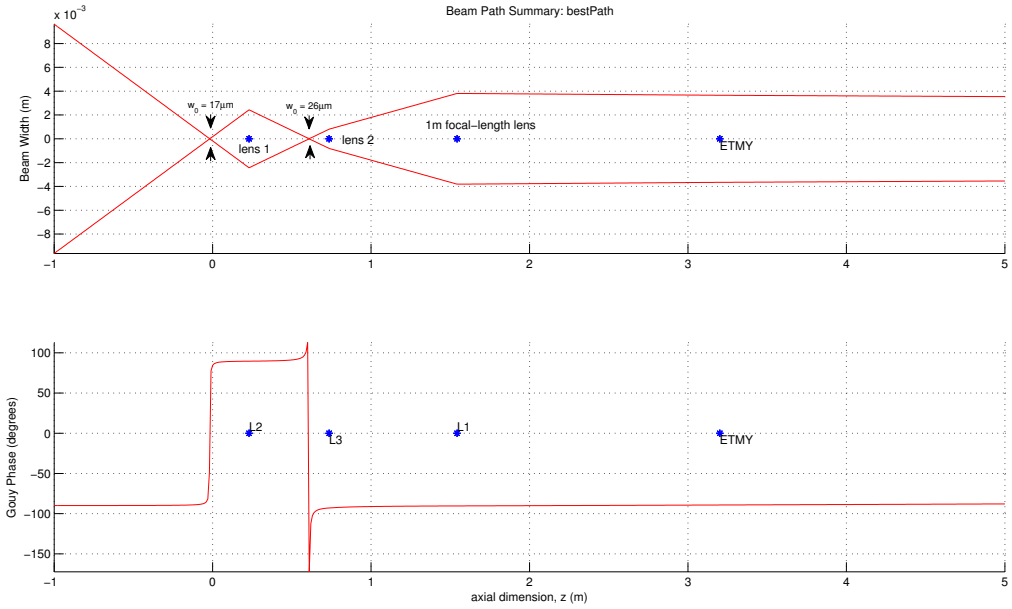

Figure 8: Beam propagation from the end of the Faraday isolator to the ETM. Mode-matching lenses are marked.

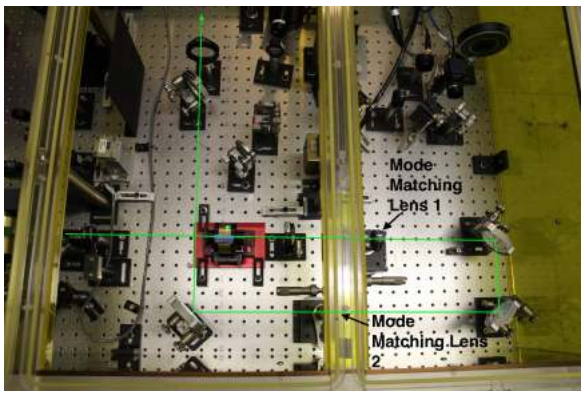

(a) Positions of the mode-matching lenses, and the path traced by the green beam before entering the FP arm cavity

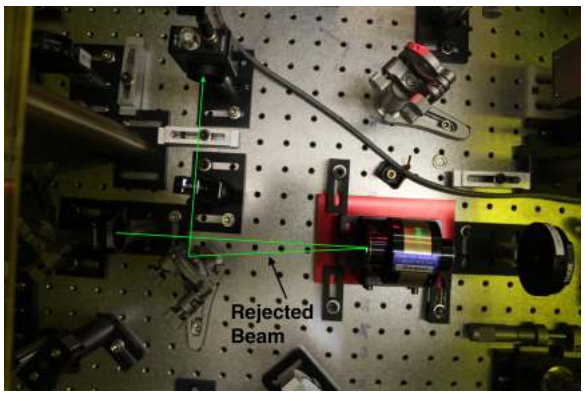

(b) Path traced by the rejected beam from the Faraday isolator

Figure 9: Physical layout of components on the endtable.

3.3 Pound-Drever-Hall (PDH) locking the auxiliary laser to the cavity

Once the green beam was mode-matched to the FP arm cavity, the next task was to use the reflected light from the cavity to lock the beam to the cavity. The scheme used to realise this is the Pound-Drever-Hall (PDH) locking technique. The PDH technique can be used to lock a cavity to a laser, or a laser to a cavity [12], depending on the point of actuation. For length-sensing and stabilization of the FP arm cavity, we require that the auxiliary laser beam be locked to the cavity, and thus, it is the latter scheme that is followed. The general layout of the PDH feedback loop implemented is shown in Figure 10.

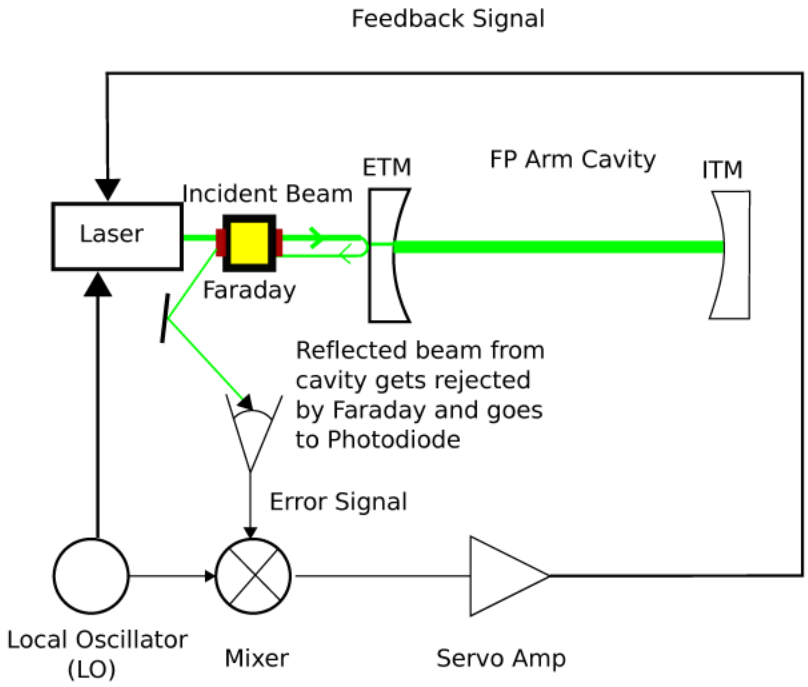

Figure 10: The general layout for locking the auxiliary laser to the FP arm cavity. Part of the incident light from the auxiliary laser is transmitted through the ETM and is resonant in the cavity, while part of it gets reflected. The reflected beam is rejected by the Faraday isolator and serves as the error signal for the PDH loop.

The crystal resonator in the auxiliary laser is mounted with a piezoelectric element. Applying a voltage to this results in a strain being set up in the crystal resonator, which in turn varies the laser frequency [9]. When the auxiliary laser beam is resonant in the FP arm cavity, the power in the light reflected from the cavity is minimum. In other words, the error signal to the PDH servo goes to zero.

LIGO has developed a Universal PDH Servo that is used for PDH locking [13], which was customised to lock the auxiliary laser to the FP arm cavity according to the scheme shown in Figure 10. It takes as inputs the error-signal and the signal from the Local Oscillator, and outputs a feedback signal which actuates on the laser to change its frequency.

The initial attempt to lock the auxiliary laser to the cavity was unsuccessful. The viewports used to monitor the resonant beam inside the FP arm cavity indicated that the beam was resonant in the TEM_{00} spatial mode, but the power in the beam was much lower than what

was expected. Furthermore, when the PDH loop was opened, much stronger 'flashes' of the TEM_{00} mode were observed, in the brief instances when the cavity alignment happened to be such that the beam was resonant in it. The problem was eventually identified to be sideband-locking, which is described below.

A mathematical model for the scheme shown in Figure 10 is given in [12]. The pertinent point is that the modulation applied by the LO results in essentially three laser beams being incident on the cavity, one at the carrier (unmodulated) frequency ω, and two sidebands, at frequencies $\omega \pm \Omega$ where Ω is the modulation frequency of the LO.

Figure 11 is a plot of the PDH error signal. It is seen that there are three zero crossings, which occur whenever either of the three incident beams is resonant inside the cavity. The zero-crossing at the origin indicates the point at which the carrier is resonant, while the other two correspond to the sidebands being resonant.

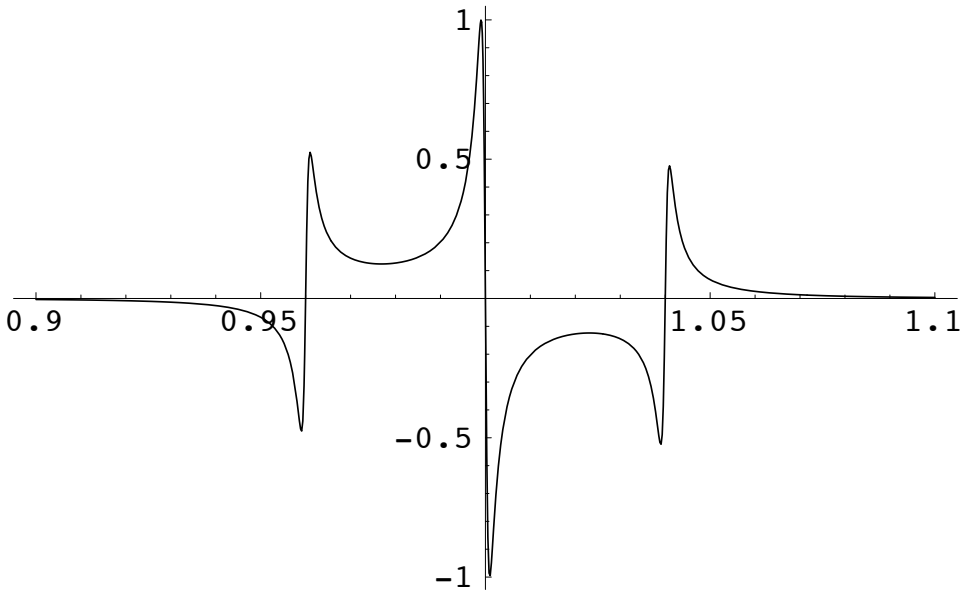

Figure 11: A plot of the PDH error signal [12]. The error signal goes to zero whenever any of the three incident beams (carrier and two sidebands) is resonant inside the cavity.

When the error signal goes to zero, the feedback loop ceases to actuate on the laser to change its frequency. As pointed out in [12], the sign of the slope of the error signal is opposite for the carrier and the sidebands. Thus, it is possible that if positive, rather than negative feedback is applied, the cavity gets locked to one of the sidebands, which holds less power than the carrier (the ratio $\frac{Power_{carrier}}{Power_{sidebands}} = \frac{J_0^2(\beta)}{J_1^2(\beta)}$ where J_0 and J_1 are the zeroth and first order Bessel functions, β is the modulation depth).

The initial PDH servo setup was not stable and susceptible to sideband locking because the following servo parameters were optimized for an auxiliary laser source which has since been replaced with a different NPRO;

- The modulation frequency, Ω. It is important that this is chosen after considering the frequency response of the laser PZT. In particular, it should avoid any of the resonances/notches in the PZT crystal's frequency response.
- The modulation depth, β.
- The demodulation phase. This determines if the mixer is able to pull out a well-defined PDH error signal, and which of the three zero-crossings the servo locks to.
- The servo gain. This determines the closed loop stability of the servo, and its ability to stay locked to the TEM_{00} mode.

The problem was rectified by empirically tuning the above parameters such that they were optimal for the new NPRO auxiliary laser. An oscilloscope was used to view the error signal, and first tuned the modulation depth and frequency such that the error signal had appreciable amplitude and had the expected shape as shown in Figure 11. The servo gain was then adjusted until we estimated from the frequency of the error signal that the servo had a bandwidth of $\approx 20kHz$, the value expected of this servo[15].

Finally, the demodulation phase was optimized by looking at the effect of placing various capacitances in the path from the LO to the Universal PDH box. To get a rough idea of how much phase a particular capacitance would introduce, we made a simulation of the situation, by modelling the function generator as having a 50Ω output impedance, and the PDH box having an input impedance of 50Ω. The circuit schematic for this is shown in Figure 12. The capacitance was then varied and the phase difference between the input and output signals was monitored. Figure 13 summarises the effect of various capacitances.

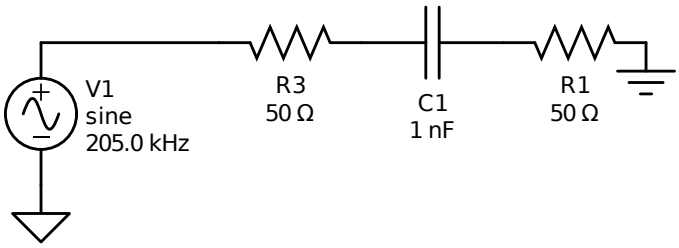

Figure 12: The circuit schematic for our model of the path from the LO to the Universal PDH box. The output impedance of the LO and the input impedance of the Universal PDH box are assumed to be 50 Ω. The value of the capacitance is swept through different values in the simulation.

We eventually chose to not have any additional capacitance in the path from the LO to the Universal PDH box as when we added a 1 nF capacitance, the amplitude of the error signal went down drastically, which suggests that we were off from the desired operating point by close to $\pi/2$ rad. From our simulation, we saw that a 1 nF capacitance introduced a phase shift of approximately $\pi/2$ rad. Hence, no additional capacitance was required to be close to the desired operating point.

We then made a measurement of the open-loop transfer function of the PDH loop, using the measurement scheme depicted in Figure 14. The results of this measurement are shown

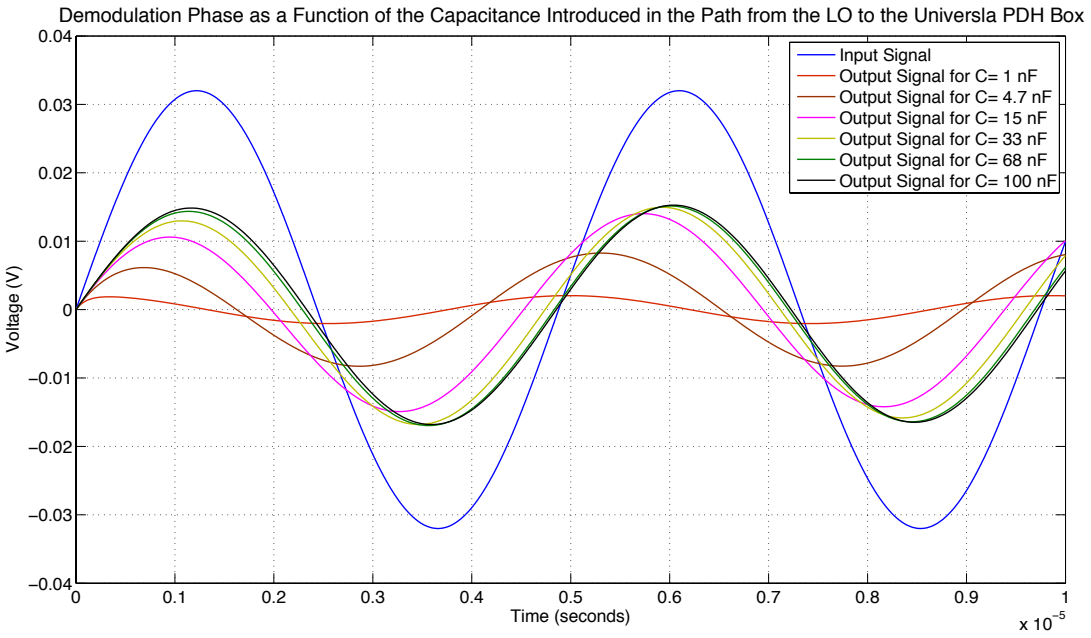

Figure 13: Results of the simulation, for various values of the capacitance C1.

in Figure 15. The unity gain frequency (UGF) of the servo as determined from this measurement is $\approx 11.7kHz$. Although this was lower than the expected UGF by a factor of 3, the servo was deemed to be sufficiently stable. It may be possible to increase the UGF by increasing the overall servo gain, but as we are already near the upper threshold of the gain permitted by the Universal PDH box, it may be required to modify the box before this change can be effected. The final values for the servo parameters at the time of writing are as follows;

- Servo gain: 7.86
- Modulation frequency: 205.02 kHz
- Modulation depth: 0.032 Vpp
- Demodulation phase: 0 rad

This concludes my discussion on mode-matching the auxiliary beam to the FP arm cavity, and setting up the servo for PDH-locking the laser to the cavity. In the following sections, I discuss the setting up of the ASC servo itself, and the associated electronics and optics.

3.4 Electronics for the ASC Servo

Figure 16 summarises the electronics involved in setting up the ASC servo. In the next few sub-sections, I discuss the various components sketched in this diagram.

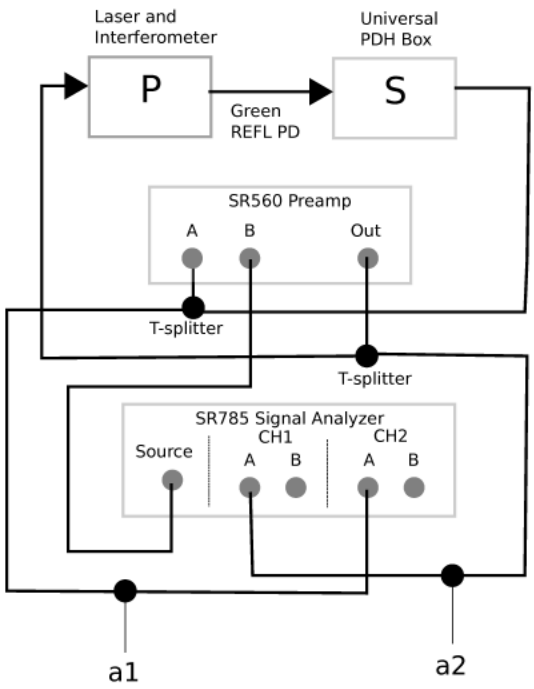

Figure 14: Block diagram of the scheme used to measure the transfer function of the PDH loop. The quantity measured by the spectrum analyzer is a1/a2, which works out to be the open loop transfer function.

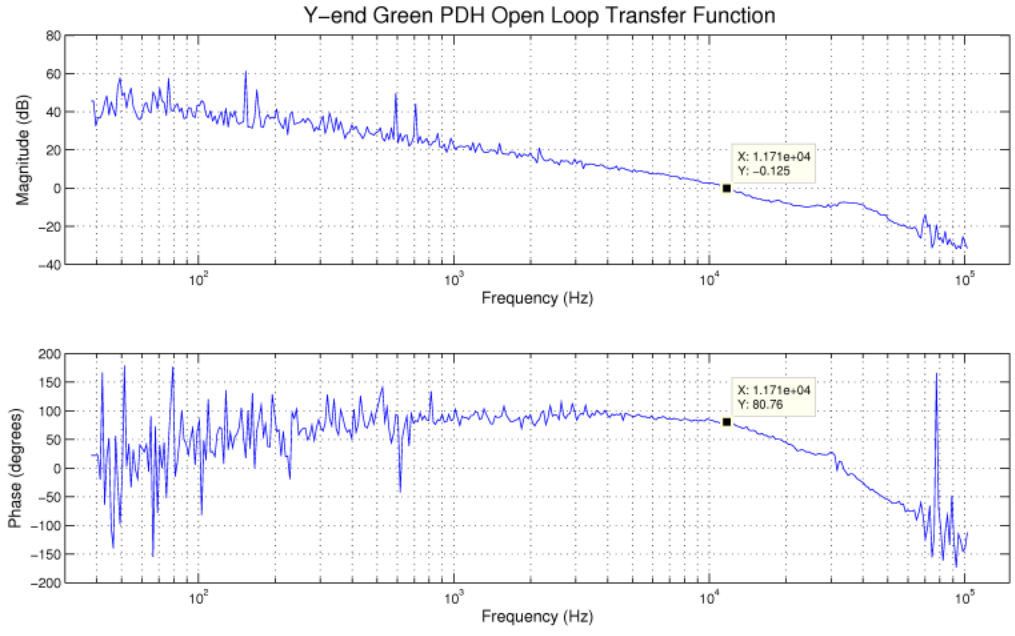

Figure 15: Measured open-loop transfer function of the PDH loop. The UGF of the loop is $\approx 11.7kHz$

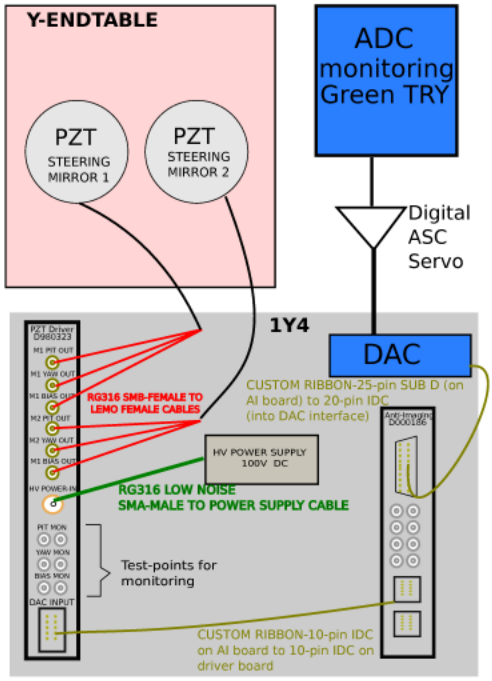

Figure 16: Wiring diagram outlining the various parts of the ASC servo. The error signal is the transmitted green beam from the arm cavity, monitored at the PSL table with a photodiode and taken into the digital domain by an Analog-to-Digital Coverter (ADC). The software ASC servo then filters the error signal, and outputs a digital feedback signal, which is converted back into an analog signal by a Digital to Analog Converter (DAC). This signal then goes through an Anti-Imaging (AI) board to a PZT driver board which then sends the feedback signal to the two piezoelectric tip-tilts on which the steering mirrors are glued.

3.4.1 PZT driver boards

In order to realise the full dynamic range of the piezoelectric tip-tilts being used (PI-S330.20L[16]), the input voltage has to vary from 0V DC to 100V DC. The DACs are only capable of supplying DC voltages between -10V DC and 10V DC. Hence, the feedback signal needs to be amplified before it is fed to the tip-tilt platforms.

It is for this purpose that the PZT driver board is used. The version employed is the D980323-Rev C [17]. The most important part of this circuit is a high-voltage amplifier, whose schematic is shown in Figure 17. The feedback signal from the DAC is fed to this amplifying stage, and the output is then fed to the tip-tilt platform.

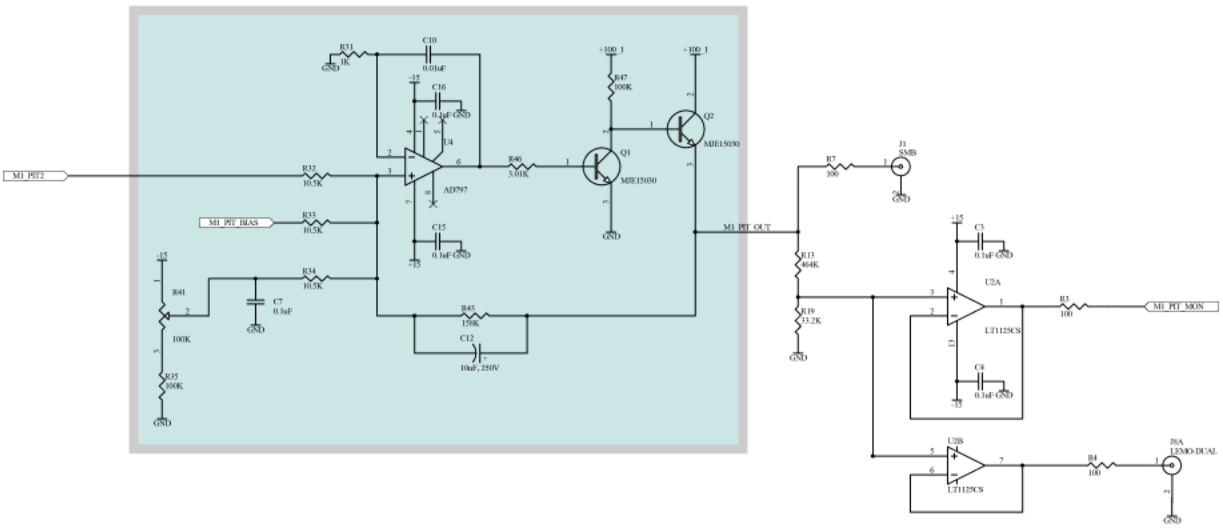

Figure 17: Amplifying stage on the PZT driver board is highlighted in blue. The 100 V DC bias voltage is supplied via a high-voltage power supply.

Neutral positioning of the tip-tilt platform is achieved when the input voltage is 50V DC [16]. In order for this to correspond to 0V DC output from the DAC, a constant voltage is always supplied to the input of the high-voltage amplifier by means of the potentiometer marked R41 in the figure.

The magnitude of this voltage depends on the gain of the amplifying stage, which is given by the expression $-\frac{R43}{R32}$. In order for the output range of the DAC to correspond to the desired output range of the driver board, i.e. 0-100 V DC, it was necessary to modify the gain of this stage. As shown in Figure 17, the gain is -15. This was changed to -5 by changing the value of R43 from $158k\Omega$ to $51k\Omega$. With this gain, the constant voltage fed to the amplifier by the voltage divider formed by R41 and R35 was -10V DC.

Once the necessary changes were made for all the channels, the output voltage was verified to be in the range 0-100 V DC for input voltages in the range -10 to 10 V DC. The input

signal was supplied using a function generator, and the output was monitored both directy using a multimeter at the output, and also by means of an oscilloscope connected to the monitor channels. These attentuated the output voltage by a factor of 14, set by the voltage divider formed by R13 and R19, such that the output can be viewed on an oscilloscope.

3.4.2 Digital-to-Analog Converter (DAC)

It was necessary to verify that the output voltage of the DAC was in the required range of -10V to 10V. The DAC cards are linked to an interface board [**?**] to which devices such as the driver board can be connected.

The DAC output is a differential one: i.e. the output voltage is not with reference to ground, but is the voltage between two output pins, one of which has been assigned 'positive' and the other 'negative' for reference [18]. Therefore, in order to measure the output voltage range of the DAC, it was necessary to use a two-channel oscilloscope, one connected to the 'positive' pin and the other to the 'negative' pin. The difference between these two signals, would then be indicative of the output range of the DAC.

The actual test was done first setting up excitation points as inputs to the DAC channels required for the ASC system in the Simulink model that runs the various servos in operation at the 40m interferometer. Then, a 3 Hz sine wave with an amplitude of 32000 counts (which is close to the maximum of 32678 for a 16-bit DAC) was set as the output by using an Arbitrary Waveform Generator. The positive and negative pins of the DAC were connected to two channels of an oscilloscope, and the math feature of the oscilloscope was used to display the difference $V_{positive} - V_{negative}$. Figure 18 is a snapshot of the output trace on the oscilloscope for $V_{positive}$, $V_{negative}$, and the difference. The output voltage range was verified to be from -10V to 10V.

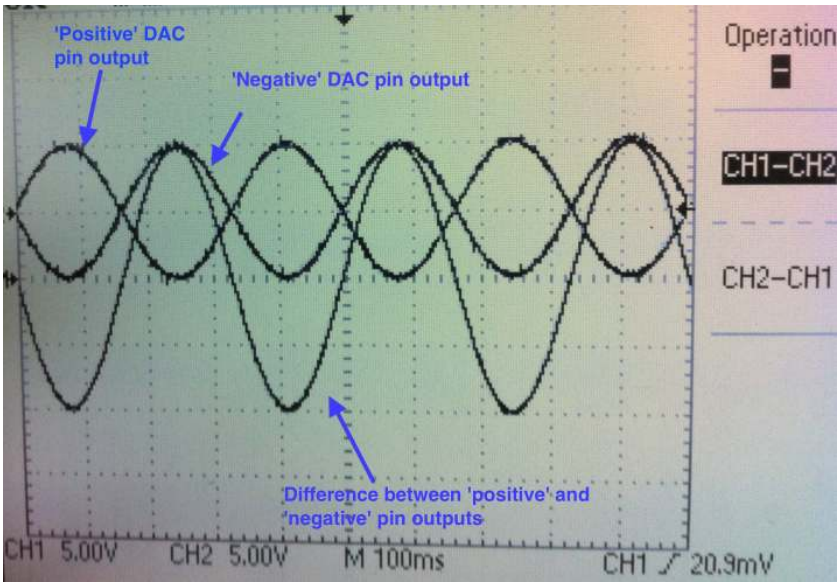

Figure 18: Results of the test to verify the output amplitude range of the DAC. Traces are labelled. The output voltage swings between -10V and 10V (both with respect to ground).

It was also necessary to measure the Power Spectral Density (PSD) of the DAC as this would determine the manner in which the Anti-Imaging (AI) board was to be configured. A DAC constructs an analog signal by switching its output between discrete voltages in steps, in a rate set by an internal clock. Thus, we would expect a peak in the PSD at the clock frequency, which needs to be removed before sending the signal out to the tip-tilt platforms, as this contribution carries no useful information. This is done by setting up notch-filters at the appropriate frequency on the AI boards. A test was done to determine what this frequency was, by measuring the PSD of a DAC channel while a 2 kHz, 1000 counts amplitude sine wave was being output from it. Figure 19 shows that there is a peak at ≈64 kHz. As I discuss in the next section, a notch filter was set-up on the AI board in order to account for this.

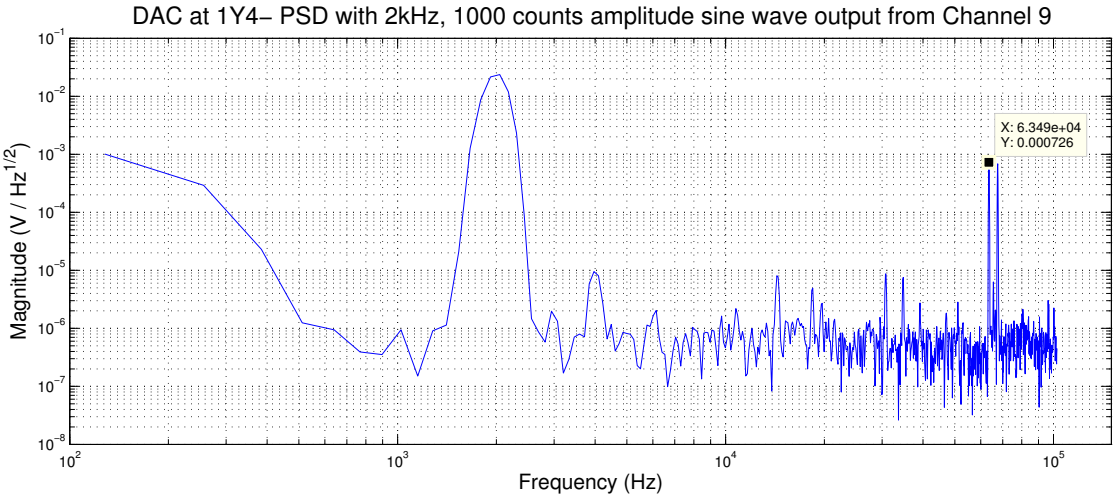

Figure 19: Power Spectral Density (PSD) of DAC channel 9 while a 2 kHz, 1000 counts amplitude sine wave was being output from it. The peak at $\approx 64kHz$ is marked.

3.4.3 Anti-Imaging (AI) Boards

As mentioned in the previous section, a DAC converts a digital signal to an analog one by changing its output in discrete steps. This inherent limitation means that reconstruction of an analog signal from a digital one can never be done perfectly, as an analog signal varies continuously, while the DAC output cannot change to reflect this continuous change any faster than the internal clock of the DAC.

Therefore, it is necessary for the output signal to be filtered in order to create a 'smoother' signal before it is fed to the PZT driver board. This is the role of an AI filter, a series of which composes the AI board. The AI board being used for implementing the ASC servo is the D000186-Rev D [19].

The AI Filter available was designed to be a 7500 Hz, 3^{rd} order, 0.5 dB ripple Chebyshev filter, with notches at 16384 Hz and 32678 Hz. The required notches for the present design, as determined from the PSD measurement of a DAC channel, were ≈ 64 kHz and ≈ 128

kHz. This change was effected by changing the resistances in the twin-T notch filter stages of the AI board.

Figure 20 is the measured transfer function of the modified AI filter. The notch at ≈ 64 kHz is visible. The spectrum analyzer used to make this measurement had an upper frequency limit of 102 kHz, and therefore the position of the notch at ≈ 128 kHz could not be verified by measurement. Nevertheless, the crucial one at ≈ 64 kHz was verified.

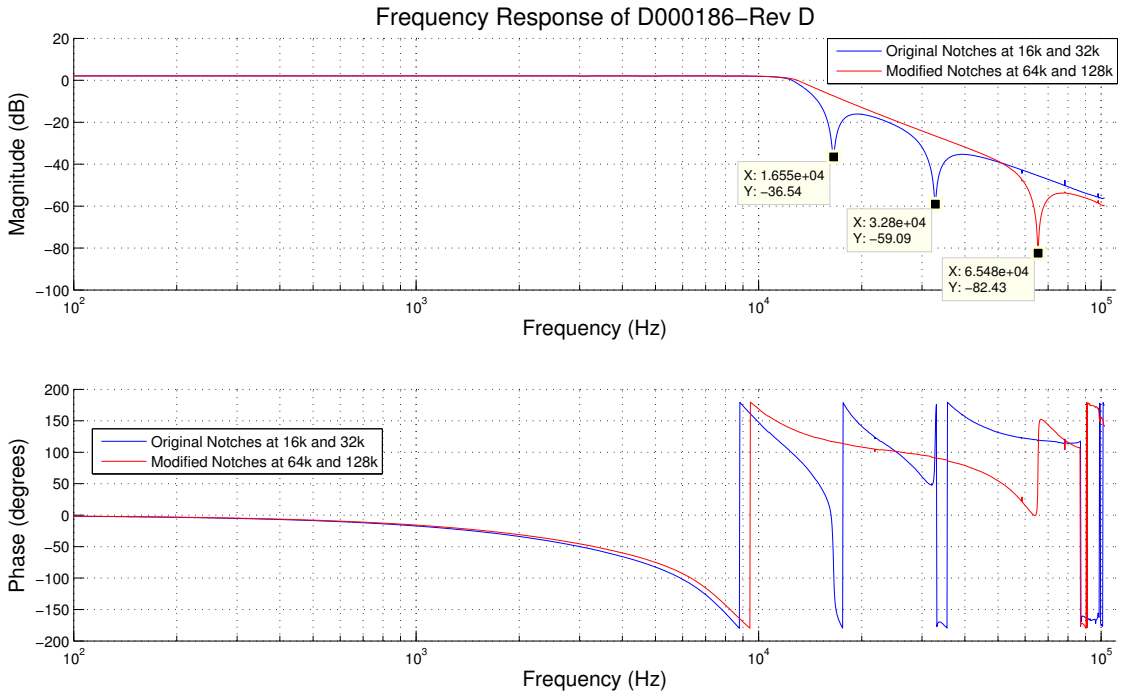

Figure 20: Measured transfer function of a modified channel on the AI board, in comparison to the original configuration. The position of the notches (both original and modified) are marked.

The other important role played by the AI board was to convert the differential output from the DAC to a single-ended output as required by the PZT driver boards. The conversion is effected using a differential line receiver IC at the input stage of the AI Filter [20]. This is important because if the differential output of the DAC is directly connected to the single-ended input on the PZT driver boards, the negative pin of the DAC will be forced to ground, which means that half of the DAC's output range, and hence the PZT's dynamic range, would be lost.

3.4.4 High Voltage DC Power Supply

The piezoelectric tip-tilts require a very steady, 100V DC bias voltage for correct operation [16]. The high-voltage amplification stage on the PZT driver boards also require a bias voltage of 100V DC [17].

In order to supply this steady high voltage, we are using a KEPCO BHK 300-130 MG high-voltage power supply [21]. The unit operates in the 'floating-output' mode, which means that the output voltage is defined as the difference between the unit's positive and negative output pins. The negative output pin is not grounded so as to allow the eurocrate in which the AI board and the PZT driver board are to be installed to define the ground for the system, and prevent the formation of ground loops.

This concludes the discussion on the electronics involved in the ASC servo signal chain.

3.5 Optics for the ASC Servo

In this section, the installation and calibration of the two steering mirrors which are a part of the ASC servo are discussed. The points of actuation for the servo will be the pitch and yaw degrees of freedom of these steering mirrors.

3.5.1 Mounting the Steering Mirrors onto the Piezoelectric Tip-Tilts

The steering mirrors are affixed to the tip-tilt platforms using superglue. Before gluing the mirror to the tip-tilt platform, both the surface of the tip-tilt and the Anti-Reflective (AR) coated side of the mirror were cleaned with methanol. The assembly is mounted in a modified Newport U100-P mirror mount [22], which was machined to accomodate the tip tilt. This was attached to a 2.5-inch optical post such that the center of the mirror is ≈4-inches from the base, which is the beam height for the auxiliary laser beam entering the arm cavity from the endtable.

The mirrors used are a 2-inch 45^oCVI mirror with High-Reflector (HR) and Anti-Reflector (AR) coatings for 532 nm and a 1-inch 45^o Laseroptik mirror with HR and AR coatings for 532nm. At the time of writing this report, these sizes were chosen by gauging the beam size on the existing steering mirrors at the endtables visually. It has to be verified that these sizes are such that the ratio of the mirror radius to the spot radius >10.

Figure 21 is a photo of the 2-inch, PZT mounted mirror, shown here in a calibration setup.

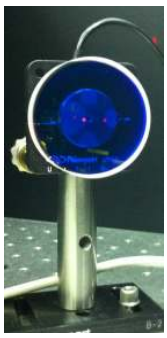

Figure 21: 2-inch CVI mirror with HR and AR coatings for 532 nm in a modified Newport U100-P mirror mount, on a 2.5-inch optical post.

3.5.2 Calibrating the Piezo-Mounted Mirror

Before the PZT-mounted mirrors were installed on the endtables, it was instructive calibrate the PZT in order to determine the range of input voltages for which the output of the tip-tilt was linear, and also to verify that all the electronics in the signal chain (PZT driver board, AI board and high-voltage power supply) were working. The calibration setup is schematically illustrated in Figure 22.

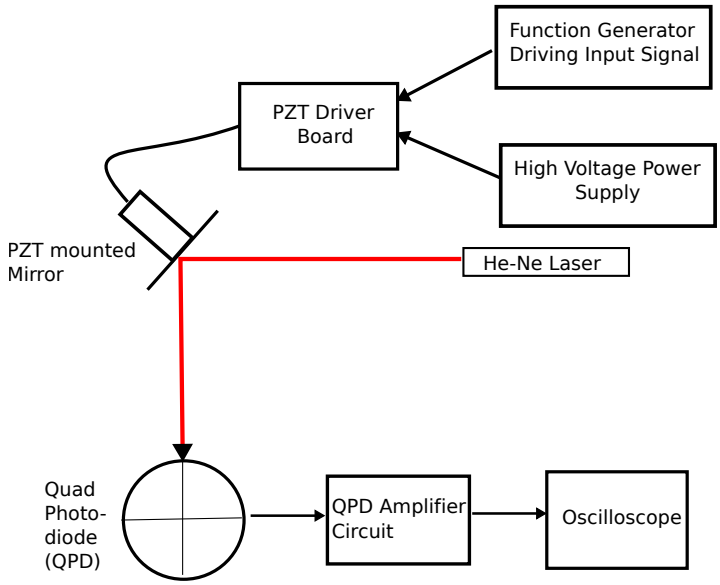

Figure 22: Schematic representation of the setup used to calibrate the PZT. The laser source is a red He-Ne laser, which is reflected by the piezo-mounted mirror onto the QPD, which can track the change in the spot position in response to the steering mirror being tilted. The input signal to the PZT is supplied by a function generator through the PZT driver board. The high-voltage power supply delivers a stable, 100V DC bias voltage.

A simple circuit consisting of four buffer amplifiers for the output from each quadrant of the QPD, and three summing amplifiers whose outputs measured the total power incident on the QPD, and the X and Y coordinates of the spot on the QPD, was constructed on a breadboard. The output of this QPD amplifier was then viewed on an oscilloscope, from which the X and Y coordinates of the spot on the QPD could be read off.

Changes in the output voltages of the X and Y coordinate amplifiers had to be related to changes in physical distances. This was done by mounting the QPD on a translational stage, and initially taking the QPD to one extreme of its sensing range for one of the coordinates (so as to avoid backlash error on the micrometer screws on the translational stage).

The QPD was then moved through to the other extreme of its sensing range in steps using the micrometer screw on the translational stage. The voltage outputs for the X and Y coordinates were noted at each step. The resulting data was fitted with an error function, and a tangent was drawn at the zero-crossing point of the error function. The slope of this tangent gives the required calibration factor in units of $\frac{Volts}{DistanceMoved}$. From these calibration plots, the linear response regime of the QPD can also be determined. The measurements

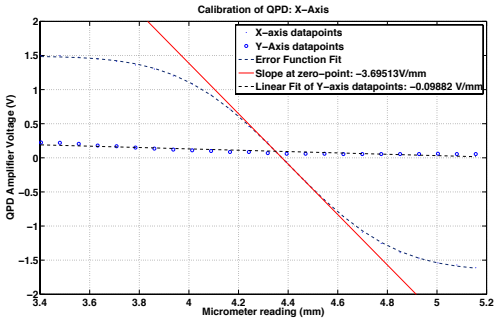

(a) QPD calibration curve for the X-coordinate. The calibration factor was determined to be -3.43 V/mm, while the linear range is when the output lies between -0.5V and 0.5V.

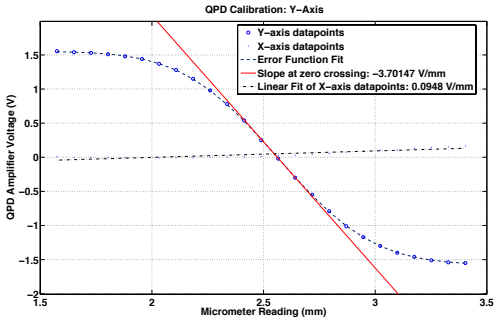

(b) QPD calibration curve for the Y-coordinate. The calibration factor was determined to be -3.41 V/mm, while the linear range is when the output lies between -0.5V and 0.5V.

Figure 23: QPD Calibration Curves

using the above calibration factor is valid, only within this linear regime.

Figure 23 shows these calibration plots for the X and Y coordinates. The calibration factors were determined to be $-3.43V/mm$ for the X coordinate and $-3.41V/mm$ for the Y coordinate. The plots also reveal that there is some coupling between the X and Y coordinates, which reflects a tilt in the QPD mounted on the translational stage. While it is difficult to eliminate this tilt completely in the physical setup, it can be accounted for in the data analysis stage.

Using the calibrated QPD, the PZT was rotated in its mount in order to coarsely decouple the pitch and yaw motion. This was done by giving a sinusoidal input to the pitch channel on the PZT driver board while the yaw channel was grounded, and noting the X and Y coordinate outputs on an oscilloscope.

Following this coarse adjustment, the PZT was calibrated. Two measurement techniques were used. In the first, the PZT was calibrated over the range of input voltages that kept the spot on the QPD in the linear regime of the QPD. To start with, the spot was centered in both X and Y coordinates on the QPD. Then, a steady DC voltage was applied in steps to the yaw input of the PZT from the function generator via the driver board, and both the X and Y coordinates of the spot on the QPD were read off (both coordinates were read off given that we expect some coupling between the pitch and yaw motion of the mirror as the PZT is imperfectly oriented within the mount). As some hysteresis was expected, the input voltage was applied in a cyclic manner. Figure 24 shows the results of this measurement.

In the second measurement, the PZT was calibrated over the full range of input voltage so as to get a rough idea as to whether the output varies linearly with the applied input voltage, and also a calibration constant that allows us to convert input voltage to output tilt. The methodology is described in the following points:

- While the output voltage of the QPD Amplifier circuit lay between -0.5V and 0.5V, its variation with the voltage applied to the PZT was approximately linear. The calibration constants are those as determined from the plots in Figure 23

- In order to keep the spot always in the linear range of the QPD, we stared with an input signal of -10V or +10V (ie. one extreme), and moved both the X and Y micrometers on the translational stage till both these coordinates were at one end of the linear range (i.e -0.5V or 0.5V). The input voltage was then increased in steps of 1V through the full range from -10V to +10V DC. The signal was applied using a function generator with the signal amplitude kept to 0, and a DC offset in the range -5V to 5V DC, which gave the desired input voltages to the PZT driver board (between -10V DC and 10V DC).
- When the output of the QPD amp reached the end of the linear regime (i.e 0.5V or -0.5V), the appropriate micrometer dial was turned on the translational stage so as to take it to the other end of the linear range, before continuing with the measurements. The distance moved was noted.
- Both the X and Y coordinates were noted in order to investigate pitch-yaw coupling.

Figures 25 and 26 show the result of the full-range calibration, and the calibration constants determined by linearly fitting the measured data. The following conclusions can be drawn from this measurement.

- The PZTs do indeed show some hysteresis. Additionally, there is also some drift, which manifested in the spot position on the QPD shifting by ≈ 0.05mm (the QPD was 40cm from the PZT mounted mirror) when the PZT was allowed to stand for approximately 1 hour with a constant input voltage.
- The PZT tilt varies linearly with the applied input voltage while it is monotonically increasing/decreasing, in the range of input voltages for which the calibration was done.
- There appears to be some small residual coupling between the pitch and yaw degrees of freedom.This could be due to the QPD's tilt or the imperfect orientation of the tip-tilt in the mount.
- The range of actuation seems to be different for the two PZTs, and also for each degree of freedom, though the measured data is consistent with the minimum range given in the datasheet (3.5 mrad for input voltages in the range -20V to 120V DC).

3.6 Designing the Control and Data-Acquisition System (CDS) for the ASC Servo

In this section, the implementation of a Control and Data-Acquisition System (CDS) that integrates the various hardware components, and implements the desired digital control loop, is discussed.

At the 40m interferometer, all of the digital control systems are implemented on multi-core computers located at the vertex and ends of the interferometer. As it often happens, control systems running on one computer may need data from other computers. Hence, the various

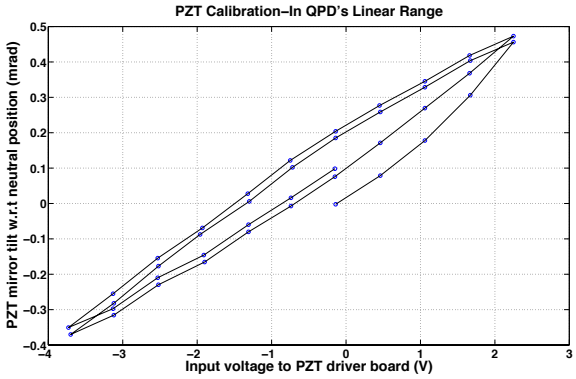

(a) Tilt in the yaw-degree of freedom as a function of input voltage applied to the yaw input of the PZT.

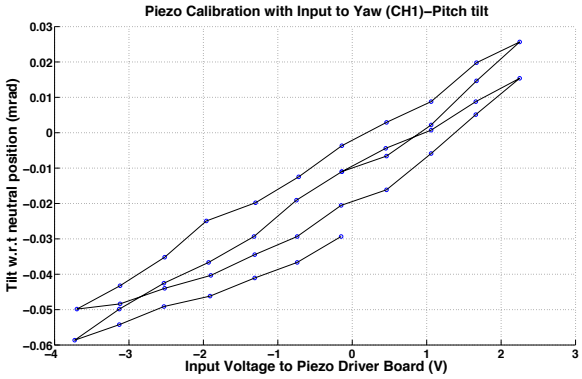

(b) Tilt in the pitch-degree of freedom as a function of input voltage applied to the yaw input of the PZT. Much noisier than the yaw-tilt, possibly because of small signal amplitude.

Figure 24: PZT Calibration Curves

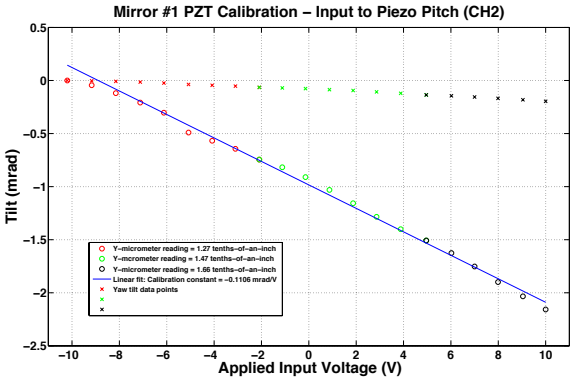

(a) Input applied to pitch degree of freedom for mirror 1.

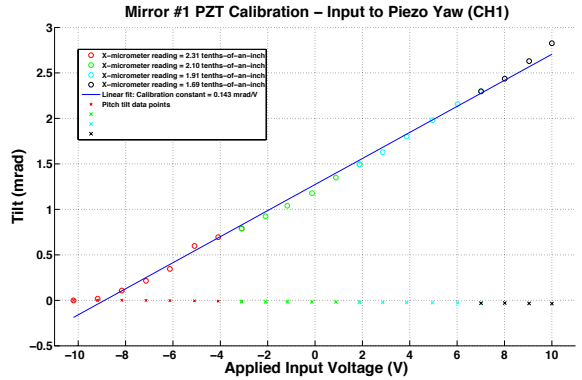

(b) Input applied to yaw degree of freedom for mirror 1.

Figure 25: Full-range calibration of PZT mounted mirror 1

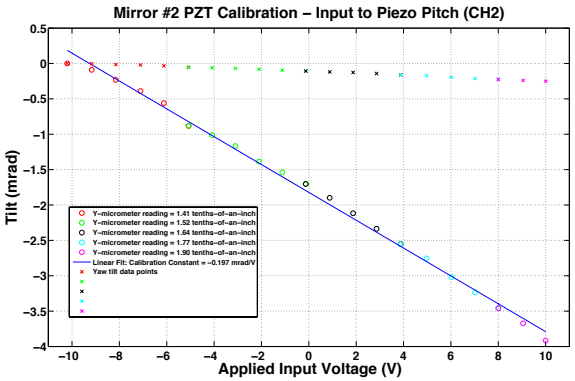

(a) Input applied to pitch degree of freedom for mirror 2.

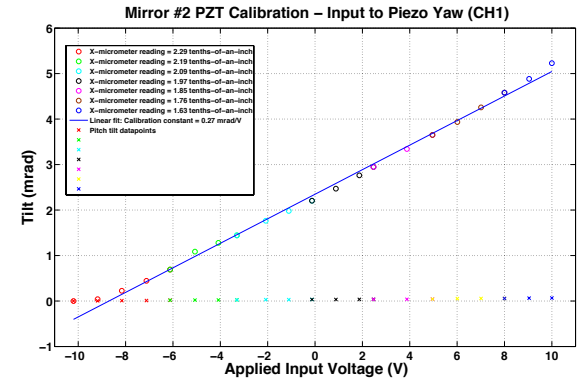

(b) Input applied to yaw degree of freedom for mirror 2.

Figure 26: Full-range calibration of PZT mounted mirror 2

control loops run within a real-time computing framework, with a single clock serving all of the computers.

The digital servos themselves are implemented as real-time C-code, generated by first constructing the appropriate SIMULINK models. This was the approach followed for the ASC servo as well. The structure of the CDS servo essentially mirrors that depicted in Figure 3. The role of the various blocks have already been explained in detail in Section 3.1, but I have briefly re-examined the signal chain, shown in Figure 27 in the context of the CDS for completeness.

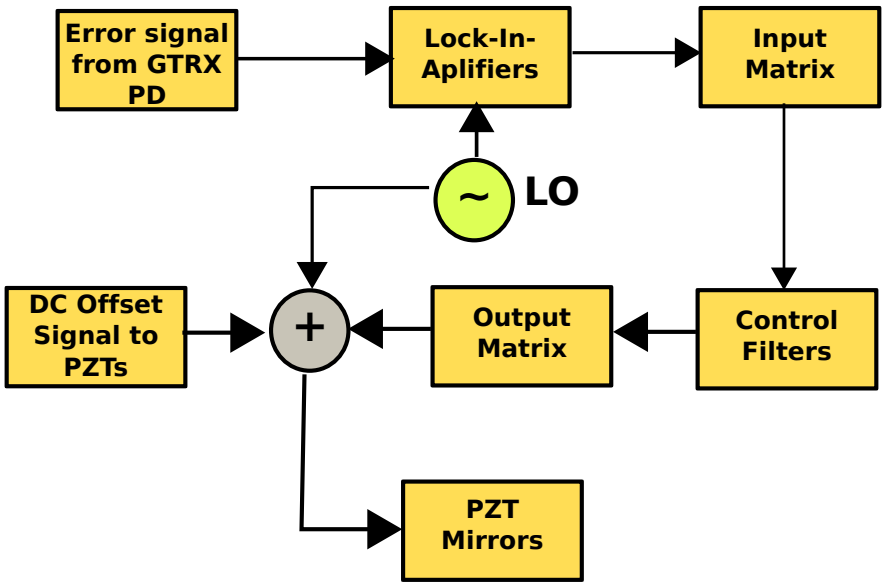

Figure 27: Schematic of the CDS signal chain. The error signal from the X-arm green transmission photodiode (GTRX PD) is acquired into the CDS and demodulated by a stage of Lock-In-Amplifiers. The demodulated signal is fed to the control filters via an Input Matrix. The feedback signal is then sent to an Output Matrix, summed with the Local Oscillator signal and a DC bias signal (if any) to the PZT mounted mirrors.

4 Measurements for Optimizing CDS Servo and Results

In this section, the various measurements made in order to optimize the ASC servo, and the results after optimization, are discussed. The measurements made for the various hardware components constituting the servo have already been discussed in detail in Section 4, and hence, this section concerns itself primarily with the CDS part of the ASC servo. The procedure consisted of optimizing the following parameters:

- The amplitude and frequency of the Local Oscillator (LO) dither signal.
- The gains and cut-off frequencies of the filters in the Lock-In-Amplifier (LIA) stage of the servo.

- Finding the appropriate control filters.
- The elements of the Input and Output matrices.
- Overall servo gain.

Of these, some parameters were optimized empirically, by tuning the parameters while the servo was on. Others, however, were optimized by first making a measurement and then choosing the parameter value appropriately. Each of these parameters is discussed in the following sub-sections.

4.1 Dither Signal Parameters

In a two-mirror cavity, misaligning the beam axis with respect to the cavity axis by either translation or rotation, couples power in the TEM_{00} mode into higher order modes. For an angular misalignment of the beam axis relative to the cavity axis by an angle a, as shown in Figure 28 the fraction of power coupled into the first higher order mode, μ is given by [4]

$$\mu = a\frac{\pi\omega_o}{\lambda} \tag{5}$$

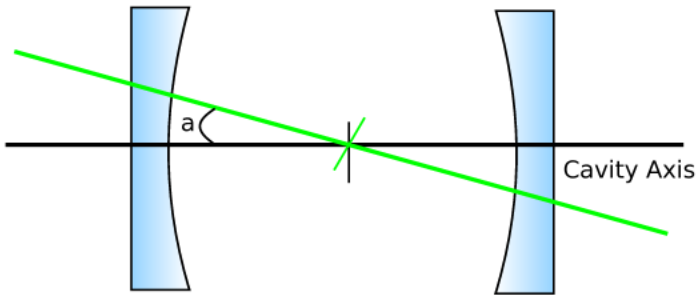

Figure 28: Angular misalignment of the beam axis with respect to the cavity axis.

Using the data from the PZT calibration, I was able to determine that voltage which when applied to the PZTs couples 10% of the power in the TEM_{00} mode to the first higher order mode (assuming a perfectly aligned beam to start with). This voltage was determined to be approximately 40 mV. The motivation behind setting the dither amplitude at this level was that the dither itself should not overly perturb a well aligned beam.

The dither frequencies were chosen after looking at the Power Spectral Density (PSD) plot of the error signal. The measured PSD is shown in Figure 29. The region in which the dither frequencies were chosen is also marked. These frequencies were chosen so as to be able to easily extract the dithered component of the error signal.

4.2 Gains and Cut-Off Frequencies of Lock-In-Amplifier Filters

A Lock-In-Amplifier essentially consists of a band-pass filter stage, a mixer, and a low-pass filter stage in series. The cutoff frequencies of the band-pass filters were chosen to be such

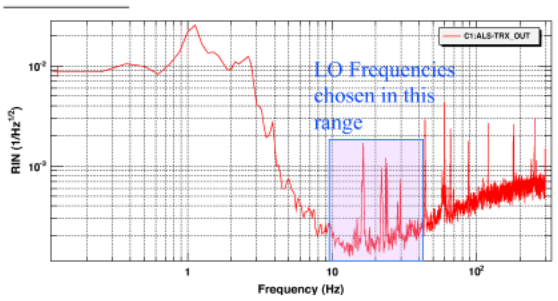

Figure 29: Power Spectral Density of the X-end Green Transmission Photodiode (GTRX) signal. Note that the Y-axis is the Relative Intensity Noise (RIN).

that the passband was 2 Hz, and centred at the LO dither frequency for that particular degree of freedom. The low-pass filters were chosen to have a cutoff frequency of 0.5 Hz.

The gains of all the filter stages were determined empirically, by monitoring the servo performance and tuning these gains. In general, it was observed that the servo was able to respond faster as the servo gain was increased, up till a point when the servo became unstable (which manifested as oscillations in the feedback signal - the numerical value of the servo gain at which this occurred was approximately 10).

Finally, the demodulation phase was set to 0 for all the degrees of freedom. This value was empirically determined, and was not tuned further as the servo performance was satisfactory with this value.

4.3 Control Filters

The control filters were chosen to be simple integrators for all the degrees of freedom, motivated by the fact that there were a number of control loops at the 40m interferometer similar in form to this particular ASC servo that employed integrators as the control filters. The gain of these filters were chosen empirically, and was set at 5.

4.4 Input and Output Matrices

The input (sensing) matrix was set as a 4 x 4 unit matrix. The output matrix elements were determined empirically. Initially, the output matrix, too, was set as a 4 x 4 unit matrix. With this diagonal output matrix, the rest of the servo parameters (filter gains) were optimized.

We then experimented by setting the off-diagonal elements to non-zero values, in an effort to account for the pitch-yaw coupling that was evident during the calibration of the PZTs. However, after considerable tweaking, no significant improvement was seen in the performance of the servo with a non-diagonal output matrix. Therefore, we reverted to a 4 x 4 unit matrix as the output matrix.

In summary, the input and output matrices used were identical and was the following:

$$\begin{bmatrix} 1 & 0 & 0 & 0 \\ 0 & 1 & 0 & 0 \\ 0 & 0 & 1 & 0 \\ 0 & 0 & 0 & 1 \end{bmatrix} \tag{6}$$

4.5 Results and Servo Performance

With the servo parameters optimized as described in the preceeding subsections, we performed a few trial runs in order to gauge the servo performance. Figure 30 is a representative plot of the servo's performance.

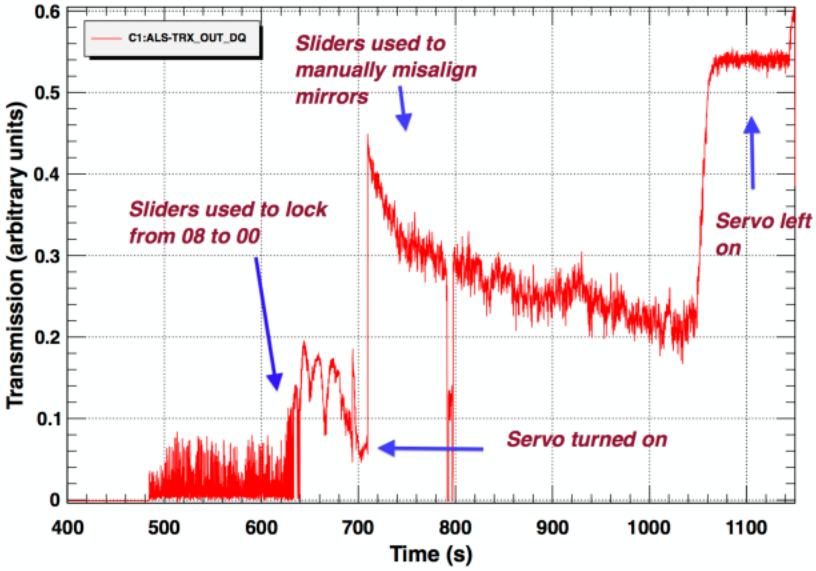

Figure 30: Performance plot for the ASC servo. Key events are marked on the plot. The test itself is described in detail below.

The test started with the cavity nominally aligned, in a TEM_{08} mode. By supplying a constant DC offset voltage to the PZTs, by means of sliders on the MEDM screen, we were able to lock the cavity to the TEM_{00} mode. Then, the servo was enabled. The green transmission from the arm cavity (measured at the PSL table) improved from approximately 0.2 to 0.5 (in arbitrary, normalized units). The servo was then turned off, and the PZT mirrors were manually misaligned by once again supplying a DC offset voltage. After the green transmission dropped to approximately 0.3, the servo was once again enabled, and the green transmission improved to approximately 0.6, which was more or less the maximum value that was attainable given the nominal alignment of the cavity itself.

5 Concluding Remarks and Future Work

The results presented in the preceeding section are representative of the general capabilities of this ASC servo. The primary design objective was to have an automated means of correcting

for small misalignments between the cavity axis and the beam axis, and to this end, the servo is effective.

However, the fact that the actuators in this servo (i.e. the PZT-mounted mirrors) are placed physically close to one another (they are approximately 30 cm apart on the endtable) means that the system is nearly degenerate - of the four available degrees of freedom, only two are, at any given time, having significant effect on the green transmission. Actuating on the remaining two degrees of freedom brings about the same effect, and hence, they are virtually redundant.

As a result, the servo is not able to restore the green transmission to the value it takes when the cavity is almost perfectly aligned, as the degenerate system of actuators simply does not have the range to correct for large angular misalignments.

Nevertheless, provided the cavity is itself nominally aligned (which can be done using ASC systems that use the 1064 nm laser), this particular ASC servo is capable of restoring the green transmission to its maximum value from slightly misaligned states.

We also tried dithering the cavity mirrors (as opposed to the PZT-mounted mirrors), in order to investigate if the degeneracy in the system could be mitigated, at least partially. However, in the few test runs I was able to perform with this configuration, no significant improvement was observed in the servo performance.

Installation of the PZT-mounted mirrors at the endtables has also allowed for the possibility of manually tuning the fine alignment of the steering mirrors, using the sliders incorporated into the CDS system (see Appendix), with much better resolution that was possible using the coarse adjustment knobs on the mirror mounts. This capability is useful when restoring the alignment of the auxiliary laser from a badly misaligned state, as once nominal alignment is restored, it is difficult to manually maximize the green transmission given the high sensitivity of the green transmission to the position of the green steering mirrors.

Some future work with regards to this servo are as follows:

- It is not clear whether the current set of servo parameters are indeed the optimal ones. In particular, optimal values for the non-diagonal elements of the output matrix have to be found.
- The performance of the servo using dithering of the cavity mirrors has to be fully investigated.
- The servo at present has a tendency of getting 'stuck' in some modes close to the TEM_{00} mode. At such times, toggling the shutter placed before the arm cavity helps the ASC servo to 'hop' to the TEM_{00} mode. This could be integrated into the scripts that presently control this ASC servo.
- The ASC servo was only be implemented for the X-arm of the 40m interferometer. The entire setup has to be replicated on the Y-arm as well.

6 Appendix

6.1 MEDM screens

In implementing the CDS part of the ASC servo, a Motif Editor and Display Manager (MEDM) was used to construct a graphical interface that made it easier to change and optimize various servo parameters. These MEDM screens essentially mirror the schematic shown in Figure 27. Figure 31 shows the various MEDM screens that constitute the servo.

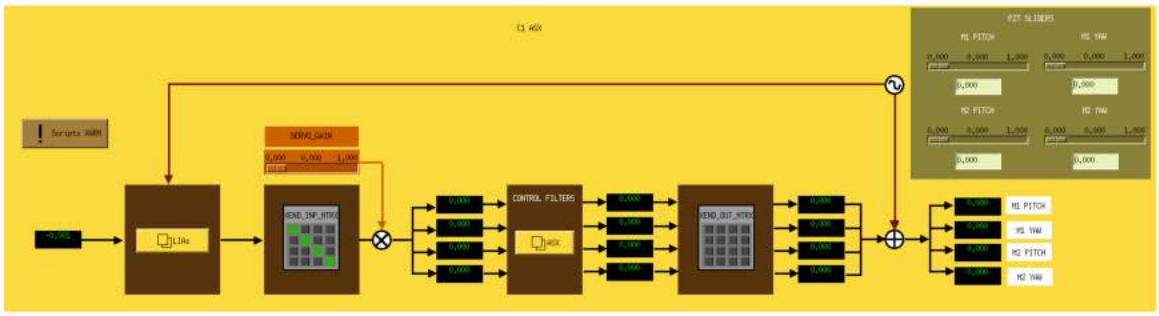

(a) Master MEDM screen showing signal chain.

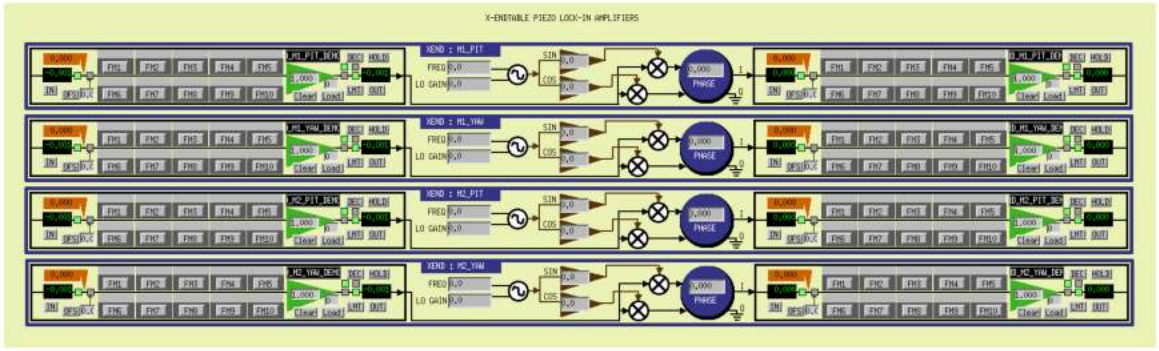

(b) Lock In Amplifiers

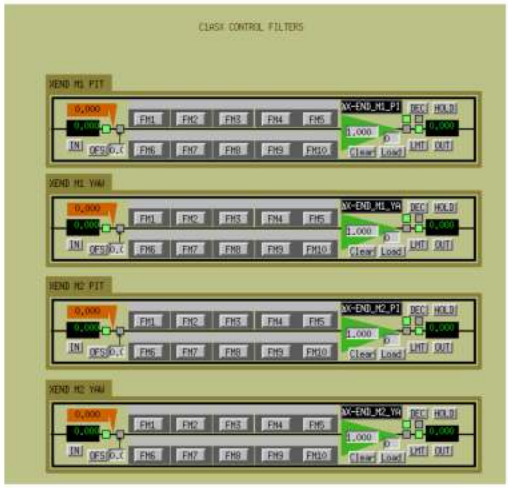

(c) Control Filters

(d) Control Filters

Figure 31: MEDM screens that constitute the ASC Servo

References

[1] Peter R. Saulson *Physics of Gravitational Wave Detection: Resonant and Interferometric Detectors* Proceedings of the XXVI SLAC Summer Institute on Particle Physics: Gravity from the Hubble Length to the Planck Length (1998)

[2] Eugene Hecht, A.R. Ganesan *Optics*. Pearson, Fourth Edition (2010).

[3] Katherine Laird Dooley, *Design and Performance of High Laser Power Interferometers for Gravitational Wave Detection* (2011) PhD Thesis

[4] Dana Z. Anderson, *Alignment of Resonant Optical Cavities* (2011) Applied Optics, Vol. 23, Issue 17, pp. 2944-2949 (1984)

[5] K. Kawabe, N. Mio, K. Tsubono, *Automatic Alignment-Control System for a Suspended Fabry-Perot Cavity* Applied Optics, Vol. 33, Issue 24, pp. 5498-5505 (1994)

[6] John Bechhoefer, *Feedback for Physicists: A Tutorial Essay on Control* Reviews Of Modern Physics, Volume 77, July 2005

[7] Matt Evans, Peter Fritschel, David McClelland, John Miller, Adam Mullavey, Daniel Shaddock, Bram Slagmolen, Sam Waldman, et. al. *Advanced LIGO Arm Length Stabilisation System Design* LIGO Technical Note T0900144-v4-D, June 2010

[8] http://nodus.ligo.caltech.edu:8080/40m/8543

[9] JDSU Continuous Wave (CW) Infrared Laser-NPRO 125/126 Series Datasheet http://www.jdsu.com/ProductLiterature/npro125126-ds-cl-ae.pdf

[10] H. Kogelnik and T. Li *Laser Beams and Resonators* LIGO Publication P660001-00-R

[11] A la Mode-mode matching and beam propagation solutions for MATLAB https://github.com/nicolassmith/alm

[12] Eric Black, *LIGO Technical Note-T980045-00-D: Notes on the Pound-Drever-Hall Technique* (1998)

[13] *Universal PDH Servo* LIGO Document D0901351-v2

[14] https://wiki-40m.ligo.caltech.edu/Advanced_Techniques/Green_Locking?action=AttachFile&do=view&target=green_optics.png

[15] K. Izumi, K. Arai, B. Barr, J. Betzwieser, A. Brooks, K. Dahl, S. Doravari, J. C.Driggers, W. Z. Korth, H. Miao, J. G. Rollins, S. Vass, D. Yeaton-Massey, and R. Adhikari *Multicolor Cavity Metrology: LIGO Document: LIGO-P1200019* (2012).

[16] Physik Instrument S330.20L Piezoelectric Tip-Tilt Platform Datasheet https://visao.as.arizona.edu/wp-content/uploads/2012/02/S-330_User_PZ149E110.pdf

[17] Mode Cleaner Steering Mirror Driver: LIGO Document: LIGO-D980323 https://dcc.ligo.org/DocDB/0020/D980323/000/D980323-C.pdf

[18] ADL General Standards 16-bit DAC Adapter Board: LIGO Document: LIGO-D0902496-VI https://dcc.ligo.org/DocDB/0006/D0902496/001/D0902496-v1.pdf

[19] Anti-Image Filter: LIGO Document: LIGO-D000186 http://www.ligo.caltech.edu/~rolf/jayfiles/drawings/D000186-D.pdf

[20] Burr-Brown Audio Differential Line Receivers Datasheet http://www.ti.com/lit/ds/sbos071/sbos071.pdf

[21] KEPCO BHK 300-130 MG High Voltage Power Supply Datasheet http://mediaserver.voxtechnologies.com/FileCache/BHK%20300-130MG.pdf

[22] U100-P Front Face for PZT mount https://wiki-40m.ligo.caltech.edu/endtable_upgrade?action=AttachFile&do=view&target=PZT+mount.pdf